

Large-wave simulation of three-dimensional, cross-shore and oblique, spilling breaking on constant slope beach

Aggelos S. Dimakopoulos, Athanassios A. Dimas*

Department of Civil Engineering, University of Patras, Patras 26500, Greece

ARTICLE INFO

Article history:

Received 2 September 2010
Received in revised form 30 March 2011
Accepted 11 April 2011
Available online 8 May 2011

Keywords:

Oblique wave propagation
Wave refraction
Spilling breaking
Surface roller
Surf zone
Large-wave simulation

ABSTRACT

In this work, the large-wave simulation (LWS) method is adapted for application in spilling wave breaking over a constant slope beach. According to LWS, large scales of velocities, pressure and free-surface elevation are numerically resolved, while the corresponding unresolved scale effects are taken into consideration by a subgrid scale (SGS) model for wave and eddy stresses. The model may be not fully applicable in very shallow water, close to the shoreline, where the unresolved, turbulent, free-surface oscillation is of the same order with the water depth. Time integration of the Euler equations is achieved by a two-stage fractional scheme, combined with a hybrid scheme for spatial discretization, consisting of finite difference and pseudospectral approximation methods. Model parameters are calibrated by comparison to available experimental data of free-surface elevation and velocities in the surf zone for cross-shore incoming waves. The action of the wave SGS stresses in the outer coastal and surf zones initiates breaking and generates appropriate vorticity, in the form of an eddy structure (surface roller), at the breaking wavefront. At incipient breaking, both advection and gravity contribute to the vorticity flux at the free surface, while only after the full development of the surface roller, the effect of advection becomes stronger. The SGS model is also utilized to simulate propagation, refraction and breaking of oblique incoming waves. The gradual breaking and dissipation of wave crests and the surface roller structure along the breaking wavefront are automatically captured without any empirical input, such as data for the roller shape or the wave propagation angle at breaking.

© 2011 Elsevier B.V. All rights reserved.

1. Introduction

Coastal engineering problems, i.e., sediment transport, coastal erosion, coastal protection, coastal structures, are directly associated with wave transformation and breaking on a beach slope. Wave transformation is a particularly complicated process in the surf zone, between the breaking point and the shore, and is characterized mainly by wave dissipation and secondary by refraction (Battjes, 1988; Peregrine, 1983).

Spilling wave breaking in the surf zone is a subject that has been studied by both numerical simulation (Bradford, 2000; Briganti et al., 2004; Christensen, 2006; Christensen and Deigaard, 2001; Dimas and Dimakopoulos, 2009; Karambas and Koutitas, 1992; Lin and Liu, 1998; Madsen et al., 1997; Musumeci et al., 2005; Schäffer et al., 1993; Torres-Freyermuth et al., 2007; Veeramony and Svendsen, 2000; Watanabe et al., 2005) and physical modeling (de Serio and Mossa, 2006; Huang et al., 2009; Longo, 2009; Ting and Kirby, 1994, 1996). The intermittent flow, which develops under the collapsing wavefront just after breaking, leads to the formation of a vortex structure, usually called “surface roller”. In the literature, methods for the numerical

simulation of spilling breakers are divided into two categories according to the treatment of the surface roller: (a) the introduction of the surface-roller dynamics effect on the flow by means of an empirical model, often called surface roller (SR) model, and (b) the full simulation of the resolved surface roller flow by a turbulence model.

According to the SR model, incipient breaking is defined by an empirical criterion, such as a critical breaking wavefront slope (Dimas and Dimakopoulos, 2009; Schäffer et al., 1993), a critical vertical velocity at the free surface (Kennedy et al., 2000) or a critical Froude number (Okamoto and Basco, 2006). Subsequently, the surface roller is sized by an empirical method (Duncan, 1983; Schäffer et al., 1993), and the introduction of the roller effect on the flow is realized either with appropriate free-surface dynamic boundary conditions (Coite and Tulin, 1994) or with additional terms in the momentum equation (Briganti et al., 2004; Madsen et al., 1997; Schäffer et al., 1993; Veeramony and Svendsen, 2000). The SR model can be combined with Boussinesq (Briganti et al., 2004; Madsen et al., 1997; Schäffer et al., 1993; Veeramony and Svendsen, 2000) or Euler (Dimas and Dimakopoulos, 2009) equations to produce very good results for two-dimensional breaking when incoming waves are propagating at a right angle to the shoreline without refraction, but it cannot be easily extended to three-dimensional breaking when incoming waves are propagating obliquely to the shoreline with refraction, since it

* Corresponding author. Tel.: +30 2610 996518; fax: +30 2610 996572.
E-mail address: adimas@upatras.gr (A.A. Dimas).

requires additional empirical parameters to identify wave direction at breaking and spanwise distribution of the surface roller.

The full simulation of the resolved surface roller flow is achieved by adopting an appropriate turbulence model, as direct numerical simulation (DNS) of turbulence still demands excessive computational resources for large-scale flows. The two most common turbulence modeling methods, i.e., the Reynolds-Averaged Navier–Stokes (RANS) equations, where all turbulent scales are treated by a closure model, and the large-eddy simulation (LES), where the large scales of turbulence are resolved while the effect of unresolved scales is modeled, have been used to simulate wave breaking.

For the case of two-dimensional turbulent flow during spilling breaking, RANS models have been applied (Bradford, 2000; Lin and Liu, 1998; Torres-Freyermuth et al., 2007) where the free surface is captured by Volume of Fluid (VOF) method (Hirt and Nichols, 1981). Vorticity and turbulent kinetic energy results indicate the formation and evolution of the surface roller in the surf zone. However, despite the diversity of turbulence closure models used, in the case of spilling breaking, comparisons with experimental data demonstrate that RANS models underestimate breaking wave height and overestimate wave dissipation in the outer surf zone. According to Bradford (2000), discretization options and boundary conditions seem to play a more important role than the type of turbulence closure model.

LES requires more computational resources than RANS, but it is expected to better capture the dynamics of spilling breakers, since large vortical structures are directly resolved. Zhao et al. (2004) and Hieu et al. (2004) compromised between low computational cost and full LES by introducing SGS models for two-dimensional flow. In both studies, VOF method is used for the free surface treatment, while turbulence is accounted for by a multiscale SGS kinetic energy model in Zhao et al. (2004) and by a Smagorinsky model in Hieu et al. (2004). Wave height in the surf zone is overestimated in Zhao et al. (2004), while the corresponding results in Hieu et al. (2004) show excellent agreement with experimental data. In the latter study, it is concluded that the effect of trapped air bubbles on wave energy dissipation during breaking is not negligible and contributes greatly to the excellent predictions. It should be noted though that the effect of two-dimensional (cylindrical) bubbles, considered in Hieu et al. (2004), on wave breaking and dissipation may be totally different than the one of three-dimensional (spherical) bubbles.

In Christensen and Deigaard (2001), fully three-dimensional LES of the surf zone dynamics over constant slope beach is performed for cross-shore wave propagation. The free surface is computed by a Marker and Cell (MAC) method (Harlow and Welch, 1965), while the Smagorinsky model is used for the SGS stresses. The effect of subgrid free-surface fluctuations is suppressed by MAC. Results show that spilling breakers develop over a beach of slope 1/20 where the larger eddy formation is a roller at the wave front with horizontal length scale equal to 1/3 of the water depth at breaking. Turbulent kinetic energy is produced at the surface roller, spanwise eddies are shed at the breaker wake and turbulent kinetic energy is diffused towards the bed. Results of free-surface elevation and wave height, at breaking and in the surf zone, are not compared to any experimental data.

In Watanabe et al. (2005), an SGS model based on renormalization group theory (RNG) and VOF computation for the free surface are employed to perform LES of cross-shore wave propagation and breaking over constant slope beach. The effect of subgrid free-surface fluctuations is not resolved by VOF. The emphasis is on the identification of coherent structures of vortices, and it is observed that, during spilling breaking over beach of constant slope 1/20, spanwise vortex filaments are shed behind the primary roller structure and are stretched to counter-rotating streamwise eddies that descend obliquely to the bed. Results of free-surface elevation and wave height, at breaking and in the surf zone, are not compared to any experimental data.

In Christensen (2006), Smagorinsky and k -equation SGS models are used to perform LES of cross-shore wave propagation and breaking over constant slope beach. The VOF method is employed for the free surface

computation but the effect of subgrid free-surface fluctuations is not resolved. Spilling breaker results, over beach of constant slope 1/35, capture turbulence production, wave dissipation and undertow flux in the surf zone but, by comparison to available experimental data (Ting and Kirby, 1994, 1996), water depth, wave crest elevation and wave height at breaking, and wave dissipation and turbulent mixing in the surf zone are overpredicted. These discrepancies are attributed to the relatively coarse grid.

Three-dimensional simulations of breaking waves with refraction are usually performed based on depth-integrated equations. Recently, Choi and Yoon (2009) introduced the numerical wave generation model of Lin and Liu (1999) in the commercial software Fluent and performed three-dimensional RANS simulations of wave breaking without and with refraction over beach of constant slope 1/34.26. The results in Choi and Yoon (2009) include reasonable wave setup, wave height and longshore current distributions in the surf zone and are compared to experimental data for cross-shore wave propagation.

The objective of this work is to present and apply a numerical model on the simulation of three-dimensional wave propagation with refraction and spilling breaking over beach of arbitrary bed shape. The model is based on the large-wave simulation (LWS) formulation, which was originally developed for two-dimensional, deep-water breaking (Dimas and Fialkowski, 2000) and is adapted here for application to three-dimensional, coastal breaking. LWS is based on the decomposition of flow scales, related to velocity, pressure and free-surface elevation, into resolved (large) and subgrid (small) scales. In LWS, the effect of SGS velocity and pressure fluctuations is treated according to LES formulation, while the effect of SGS free-surface fluctuations is also introduced in the flow equations by using a boundary-fitted transformation. The latter is in contrast to pure LES where the particular (MAC or VOF) free surface treatment does not allow for the effect of SGS free-surface fluctuations during breaking to be accounted for. Another advantage of LWS is that no special boundary conditions are required to incorporate breaking generated turbulence (Brocchini and Peregrine, 2001a, 2001b), since SGS free-surface fluctuations are included in the flow equations.

The desirable characteristics of LWS for three-dimensional breaking are: (a) automatic activation of breaking model at incipient breaking without additional information about wave direction, (b) prediction of surface roller formation after breaking and wave dissipation in the surf zone, and (c) no use of free surface treatment methods like MAC and VOF that are expensive for three-dimensional simulations. Initially, it is desired to study the net effect of the breaking model without the effect of bed resistance, therefore, SGS terms are introduced in the Euler equations. In the next three sections, the LWS formulation, the SGS stress model and the numerical solution scheme are presented, followed by results and conclusions.

2. LWS formulation

The formulation is based on the three-dimensional Euler equations of incompressible flow and the fully nonlinear free-surface boundary conditions. First, a σ -type coordinate transformation is applied to the governing equations to get a time-independent flow domain, and, subsequently, a filtering operation is performed to obtain the equations for the resolved scales.

For three-dimensional flow, the continuity equation is

$$\frac{\partial u_j}{\partial x_j} = 0 \quad (1)$$

and the Euler equations, in conservative form, are

$$\frac{\partial u_i}{\partial t} + \frac{\partial (u_i u_j)}{\partial x_j} = - \frac{\partial p}{\partial x_i} \quad (2)$$

where $i, j = 1, 2, 3$ hereafter, t is the time variable, x_i are the coordinates (x_1 is in the cross-shore direction, x_2 is in the longshore direction, and x_3 is in the vertical direction, where $x_3 = 0$ is the still water level, as shown in Fig. 1), u_i are the velocity components and p is the dynamic pressure. All variables have been rendered dimensionless with respect to inflow depth d , gravitational acceleration g and fluid density ρ .

Neglecting surface tension effect, the nonlinear kinematic and dynamic boundary conditions at the free surface, $x_3 = \eta(x_1, x_2, t)$, respectively, are

$$u_3 = \frac{d\eta}{dt} = \frac{\partial\eta}{\partial t} + u_k \frac{\partial\eta}{\partial x_k} \quad p = \frac{\eta}{F^2} \quad (3)$$

where $k = 1, 2$ hereafter, η is the free-surface elevation and $F = U_1 / \sqrt{gd_1}$ is the Froude number at inflow. In the present work, velocities are rendered dimensionless by $U_1 = \sqrt{gd_1}$, therefore, $F = 1$. The non-penetration boundary condition at the bottom, $x_3 = -d(x_1, x_2)$, is

$$u_3 + u_k \frac{\partial d}{\partial x_k} = 0 \quad (4)$$

where d is the water depth.

Since the free-surface elevation, η , is function of time, the flow domain is time-dependent. A boundary-fitted transformation is introduced to obtain a time-independent computational domain and facilitate filtering of the flow equations according to the LWS formulation (Dimas and Fialkowski, 2000). The transformed coordinates are

$$s_1 = x_1 \quad s_2 = x_2 \quad s_3 = \frac{2x_3 + d - \eta}{d + \eta} \quad (5)$$

so that $x_3 \in [-d(x_1, x_2), \eta(x_1, x_2, t)]$ is mapped into $s_3 \in [-1, +1]$. The form of the above transformation implies that it cannot be applied on plunging wave breaking.

Application of transformation (5) on Eqs. (1) and (2) results into the transformed flow equations

$$\frac{\partial u_k}{\partial s_k} + \frac{2}{d + \eta} \frac{\partial u_3}{\partial s_3} - \frac{2}{d + \eta} r_k \frac{\partial u_k}{\partial s_3} = 0 \quad (6)$$

and

$$\frac{\partial u_i}{\partial t} - \frac{1 + s_3}{d + \eta} \frac{\partial \eta}{\partial t} \frac{\partial u_i}{\partial s_3} + \frac{\partial(u_i u_k)}{\partial s_k} + \frac{2}{d + \eta} \frac{\partial(u_i u_3)}{\partial s_3} - \frac{2}{d + \eta} r_k \frac{\partial(u_i u_k)}{\partial s_3} = R_i \quad (7)$$

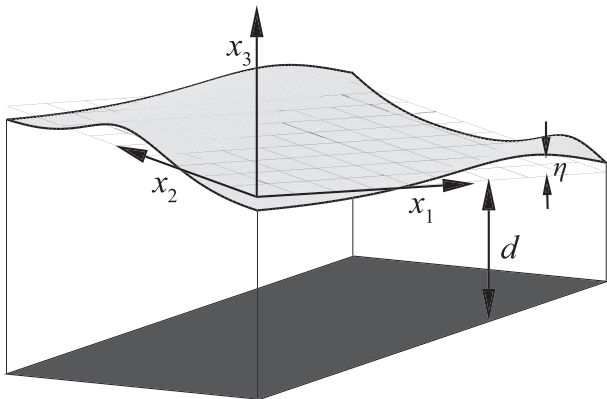


Fig. 1. Typical computational domain of coastal flow induced by wave propagation.

where

$$R_k = -\frac{\partial p}{\partial s_k} + \frac{2}{d + \eta} r_k \frac{\partial p}{\partial s_3} \quad R_3 = -\frac{2}{d + \eta} \frac{\partial p}{\partial s_3} \quad (8)$$

and

$$r_k = \frac{1 + s_3}{2} \frac{\partial \eta}{\partial s_k} - \frac{1 - s_3}{2} \frac{\partial d}{\partial s_k} \quad (9)$$

is a parameter that varies linearly, with respect to s_3 , between $\partial d / \partial s_k$, at $s_3 = -1$, and $\partial \eta / \partial s_k$, at $s_3 = 1$.

After the transformation, boundary conditions (3) and (4) are applied at $s_3 = 1$ (free surface) and $s_3 = -1$ (bottom), respectively, and become

$$u_3 = \frac{\partial \eta}{\partial t} + r_k u_k \quad p = \frac{\eta}{F^2} \quad (10)$$

and

$$u_3 + r_k u_k = 0 \quad (11)$$

The decomposition of flow variables in resolved (large) and subgrid (small) scales is achieved by a volume filtering operation for velocities and pressure, as in LES, and a surface filtering operation for the free-surface elevation, which is exclusive to LWS. Therefore, each flow variable, f , is decomposed into resolved, \bar{f} , and subgrid, f' , scales (see Fig. 2 for η).

Application of the filtering operation on Eqs. (6) and (7) results into the governing equations for the resolved scales. The filtering procedure takes into account the following:

- i. $2 / (d + \eta) \approx 2 / (d + \bar{\eta})$ and, subsequently, $\overline{2f / (d + \eta)} = 2\bar{f} / (d + \bar{\eta})$ since $|\eta'| \ll |d + \eta|$. This assumption may not be satisfied in very shallow water close to the shoreline.
- ii. $\overline{u_i (\partial \eta / \partial s_j)} - \bar{u}_i (\partial \bar{\eta} / \partial s_j) \approx 0$ as shown in Dimas and Fialkowski (2000).
- iii. $\overline{s_3 f} = s_3 \bar{f}$ when a cut-off Chebyshev filter is used in the vertical direction (Dimakopoulos, 2009).

The resulting continuity and Euler equations for the resolved scales, respectively, are

$$\frac{\partial \bar{u}_k}{\partial s_k} + \frac{2}{d + \bar{\eta}} \frac{\partial \bar{u}_3}{\partial s_3} - \frac{2}{d + \bar{\eta}} \bar{r}_k \frac{\partial \bar{u}_k}{\partial s_3} = 0 \quad (12)$$

and

$$\frac{\partial \bar{u}_i}{\partial t} - \frac{1 + s_3}{d + \bar{\eta}} \frac{\partial \bar{\eta}}{\partial t} \frac{\partial \bar{u}_i}{\partial s_3} + \frac{\partial(\bar{u}_i \bar{u}_k)}{\partial s_k} + \frac{2}{d + \bar{\eta}} \frac{\partial(\bar{u}_i \bar{u}_3)}{\partial s_3} - \frac{2}{d + \bar{\eta}} \bar{r}_k \frac{\partial(\bar{u}_i \bar{u}_k)}{\partial s_3} = \bar{R}_i - \frac{\partial \tau_{ik}}{\partial s_k} - \frac{2}{d + \bar{\eta}} \frac{\partial \tau_{i3}}{\partial s_3} + \frac{1 + s_3}{d + \bar{\eta}} \frac{\partial \tau_{i3}^n}{\partial s_3} - \frac{1 - s_3}{d + \bar{\eta}} \frac{\partial \tau_{ik}}{\partial s_3} \frac{\partial d}{\partial s_k} \quad (13)$$

where

$$\bar{R}_k = -\frac{\partial \bar{p}}{\partial s_k} + \frac{2}{d + \bar{\eta}} \bar{r}_k \frac{\partial \bar{p}}{\partial s_3} \quad \bar{R}_3 = -\frac{2}{d + \bar{\eta}} \frac{\partial \bar{p}}{\partial s_3} \quad (14)$$

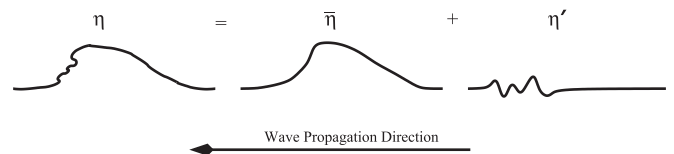


Fig. 2. Free surface decomposition for a spilling breaker.

and

$$\bar{r}_k = \frac{1 + s_3}{2} \frac{\partial \bar{\eta}}{\partial s_k} - \frac{1 - s_3}{2} \frac{\partial d}{\partial s_k} \quad (15)$$

while

$$\tau_{ij} = \overline{u_i u_j} - \bar{u}_i \bar{u}_j \quad (16)$$

are the eddy SGS stresses, as in LES, and

$$\tau_{i3}^\eta = \overline{u_i u_k} \frac{\partial \bar{\eta}}{\partial s_k} - \bar{u}_i \bar{u}_k \frac{\partial \bar{\eta}}{\partial s_k} + u_i \frac{\partial \bar{\eta}}{\partial t} - \bar{u}_i \frac{\partial \bar{\eta}}{\partial t} + p \frac{\partial \bar{\eta}}{\partial s_i} - \bar{p} \frac{\partial \bar{\eta}}{\partial s_i} \quad (17)$$

are the wave SGS stresses, which are exclusive to LWS. The eddy SGS stresses, τ_{ij} , correspond to the effect of the unresolved velocity scales, while the wave SGS stresses, τ_{ij}^η , represent the combined effect of unresolved free surface and velocity scales. The wave SGS stresses have non-zero values only when $j=3$, therefore, they act on the $s_1 - s_2$ plane.

Accordingly, the filtered boundary conditions at the free surface ($s_3 = 1$) and the bottom ($s_3 = -1$), respectively, become

$$\bar{u}_3 = \frac{\partial \bar{\eta}}{\partial t} + \bar{r}_k \bar{u}_k \quad \bar{p} = \frac{\bar{\eta}}{F^2} \quad (18)$$

and

$$\bar{u}_3 + \bar{r}_k \bar{u}_k = 0 \quad (19)$$

The inverse application of transformation (5) on Eqs. (12) and (13) gives the corresponding governing equations for the resolved flow scales in physical coordinates

$$\frac{\partial \bar{u}_j}{\partial x_j} = 0 \quad (20)$$

$$\frac{\partial \bar{u}_i}{\partial t} + \frac{\partial (\bar{u}_i \bar{u}_j)}{\partial x_j} = -\frac{\partial \bar{p}}{\partial x_i} - \frac{\partial \tau_{ij}}{\partial x_j} + \frac{x_3 + d}{d + \bar{\eta}} \frac{\partial}{\partial x_3} \left(\tau_{i3}^\eta - \tau_{ik} \frac{\partial \bar{\eta}}{\partial x_k} \right) \quad (21)$$

It is, therefore, deduced that the SGS free surface effect cannot be obtained by direct filtering of the flow equations without the boundary transformation step.

3. SGS model

In the present work, Smagorinsky eddy viscosity models (Rogallo and Moin, 1984) are used for the computation of the eddy and wave SGS stresses in Eq. (13).

In particular, the model for the eddy SGS stresses is

$$\tau_{ij} = -2\nu_\tau \bar{S}_{ij} = -2C^2 \Delta^2 |\bar{S}| \bar{S}_{ij} \quad (22)$$

where C is the model parameter, $\Delta = (\Delta_1 \Delta_2 \Delta_3)^{1/3}$ is the smallest resolved scale based on the grid size Δ_i , S_{ij} is the strain-rate tensor of resolved scales

$$\bar{S}_{ij} = \frac{1}{2} \left(\frac{\partial \bar{u}_i}{\partial s_j} + \frac{\partial \bar{u}_j}{\partial s_i} \right) \quad (23)$$

and $|\bar{S}| = \sqrt{\bar{S}_{ij} \bar{S}_{ij}}$ is its magnitude.

The model for the wave SGS stresses, based on the one presented in Dimas and Fialkowski (2000), is

$$\tau_{ij}^\eta = -2\nu_\tau \bar{S}_{ij}^\eta = -2(C^\eta)^2 \bar{\Delta}^2 |\bar{S}^\eta| \bar{S}_{ij}^\eta \quad (24)$$

where C^η is the model parameter and S_{ij}^η is a modified strain-rate tensor of resolved scales

$$\bar{S}_{ij}^\eta = \delta_{3j} S_{ik} \left| \frac{\partial \bar{\eta}}{\partial s_k} \right| \quad (25)$$

where δ_{ij} is the Kronecker delta, and the absolute value of the free surface slope ensures the model invariance on the wave propagation direction.

The value of parameter $C=0.1$ is set according to the usual practice in LES, while the value of parameter C^η will be set after model calibration with experimental data according to the procedure described in the calibration section.

4. Numerical implementation

A two-stage, fractional time-step scheme is used for the temporal discretization of the flow equations, while a hybrid scheme, consisting of central finite differences in s_1 and pseudospectral methods in s_2 (Fourier) and s_3 (Chebyshev), is used for the spatial discretization.

First, a transformed velocity, \bar{v}_i , is defined

$$\bar{v}_1 = \bar{u}_1 \quad \bar{v}_2 = \bar{u}_2 \quad \bar{v}_3 = \bar{u}_3 - \bar{r}_k \bar{u}_k \quad (26)$$

and introduced to Eqs. (12) and (13), which written in rotational form, respectively, become

$$\partial_j^T \bar{v}_j + \frac{2}{d + \bar{\eta}} \bar{v}_k \frac{\partial \bar{r}_k}{\partial s_3} \quad (27)$$

and

$$\frac{\partial \bar{v}_i}{\partial t} = \epsilon_{ijm} \bar{v}_j \bar{S}_m + \bar{A}_i + \bar{T}_i + \partial_i^T \bar{\Pi} \quad (28)$$

where ϵ_{ijm} is the alternating unit tensor (also called the permutation or the Levi-Civita tensor),

$$\partial_1^T = \frac{\partial}{\partial s_1} \quad \partial_2^T = \frac{\partial}{\partial s_2} \quad \partial_3^T = \frac{2}{d + \bar{\eta}} \frac{\partial}{\partial s_3} \quad (29)$$

is a modified gradient operator,

$$\bar{S}_i = \epsilon_{ijm} \partial_j^T \bar{v}_m \quad (30)$$

is the transformed vorticity, \bar{T}_i are the SGS terms of Eq. (13),

$$\bar{A}_k = \frac{1 + s_3}{d + \bar{\eta}} \frac{\partial \bar{\eta}}{\partial t} \frac{\partial \bar{u}_k}{\partial s_3} + \frac{2}{d + \bar{\eta}} \bar{r}_k \frac{\partial \bar{p}}{\partial s_3} \quad (31)$$

$$\bar{A}_3 = \frac{1 + s_3}{d + \bar{\eta}} \frac{\partial \bar{\eta}}{\partial t} \frac{\partial \bar{u}_3}{\partial s_3} - \frac{\partial (\bar{r}_k \bar{v}_k)}{\partial t} - \bar{v}_j \partial_j^T (\bar{r}_k \bar{v}_k) \quad (32)$$

are the remaining nonlinear terms of Eq. (13) and

$$\bar{\Pi} = \bar{p} + \frac{1}{2} \bar{v}_j \bar{v}_j \quad (33)$$

is the transformed dynamic pressure head. The flow equations are expressed in rotational form, which ensures that the numerical application of pseudospectral approximation in the spatial discretization is not unconditionally unstable (Gottlieb and Orszag, 1977).

The boundary conditions (18) and (19), at the free surface ($s_3 = 1$) and the bottom ($s_3 = -1$), respectively, become

$$\bar{v}_3 = \frac{\partial \bar{\eta}}{\partial t} \quad \bar{\Pi} = \frac{\bar{\eta}}{F^2} + \frac{1}{2} \bar{v}_j \bar{v}_j \quad (34)$$

and

$$\bar{v}_3 = 0 \tag{35}$$

At the first stage of the fractional time-step, the nonlinear and the SGS terms of Eq. (28) are treated by an explicit scheme

$$\frac{\hat{v}_i - \bar{v}_i^n}{\Delta t} = [\epsilon_{ijm} \bar{v}_j \bar{v}_m + \bar{A}_i + \bar{T}_i]^n \tag{36}$$

to obtain the intermediate velocity, \hat{v}_i , while at the second stage of the time-step, the pressure head terms of Eq. (28) are treated by an implicit scheme

$$\frac{\bar{v}_i^{n+1} - \hat{v}_i}{\Delta t} = -[\partial_i^T \bar{\Pi}]^{n+1} \tag{37}$$

to update the velocity. Substitution of Eq. (37) into Eq. (27) results in a generalized Poisson equation for the pressure head, which is written in the form

$$\frac{\partial^2 \bar{\Pi}}{\partial s_1^2} + \frac{\partial^2 \bar{\Pi}}{\partial s_2^2} + \frac{4}{d^2} \frac{\partial^2 \bar{\Pi}}{\partial s_3^2} = -\frac{2}{d + \bar{\eta}} \frac{\partial \bar{r}_k}{\partial s_3} \frac{\partial \bar{\Pi}}{\partial s_k} + \left(\frac{4}{d^2} - \frac{4}{(d + \bar{\eta})^2} \right) \frac{\partial^2 \bar{\Pi}}{\partial s_3^2} + \frac{1}{\Delta t} \left(\partial_j^T \hat{v}_j + \frac{2}{d + \bar{\eta}} \hat{v}_k \frac{\partial \bar{r}_k}{\partial s_3} \right) = \bar{G} \tag{38}$$

to facilitate its numerical solution by an iterative scheme. After the computation of \hat{v}_i at the first stage of the time-step, pressure head, $\bar{\Pi}$, is computed by Eq. (38) and substituted into Eq. (37) to obtain velocity, \bar{v}_i^{n+1} , at the next time-step. The free-surface elevation is obtained by the kinematic free-surface boundary condition (34) using an implicit scheme since the velocity field is updated.

In the present work, wave propagation over constant slope beach is simulated, and a sketch of the corresponding computational domain is shown in Fig. 3. Second-order Stokes waves of period T and height H_I are generated at the inflow boundary, $s_1 = 0$, where the water depth is d_I . A region of length L_I and constant depth d_I , after the inflow boundary, is followed by the region of bed of constant slope $\tan\beta$ and then a region of length L_E and constant depth d_E , before the outflow boundary. The formulation allows the outflow depth d_E to be small but nonzero. An absorption zone of length $L_A < L_E$ is placed just upstream of the outflow boundary, as in Dimas and Dimakopoulos (2009), to ensure that waves are exiting without reflections, while periodic conditions are applied at the lateral boundaries in s_2 .

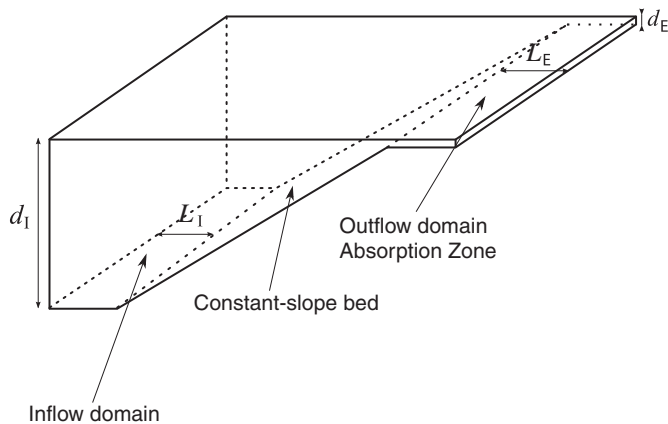


Fig. 3. Computational domain for simulation of waves over constant slope beach. The domain consists of a constant depth inflow region, a constant slope region and a constant depth outflow region where the absorption zone is placed.

According to the hybrid scheme for the spatial discretization, each resolved flow variable, \bar{f} , is approximated as

$$\bar{f}_l(s_2, s_3, t) = \sum_{m=-M/2}^{M/2-1} \sum_{n=0}^N \check{f}_{l,mn}(t) \exp\left(-2\pi i \frac{ms_2}{L_2}\right) T_n(s_3) \tag{39}$$

where $\check{f}_{l,mn}$ is the Fourier–Chebyshev transformation of \bar{f}_l , $l \in [0, L]$ is the index and L is the number of finite-differences nodes, $L_1 = L\Delta_1$ is the length of the computational domain in s_1 , M is the maximum order of Fourier modes, $L_2 = M\Delta_2$ is the length of the computational domain in s_2 , T_n is the Chebyshev polynomial of order $n \in [0, N]$ and N is the maximum order of Chebyshev polynomials. The transformations (forward and inverse) between physical and spectral space are performed by a Fast Fourier Transform algorithm (Press et al., 1992).

The application of discretization (39) on Eq. (38) results in the following discrete equation for the Fourier–Chebyshev transformation of pressure head

$$\frac{\check{\Pi}_{l+1,mn} - 2\check{\Pi}_{l,mn} + \check{\Pi}_{l-1,mn}}{\Delta_1^2} - \left(\frac{2\pi m}{L_2}\right)^2 \check{\Pi}_{l,mn} + \frac{4}{d^2} \frac{1}{c_n} \sum_{p=n+2}^N p(p-n^2) \check{\Pi}_{l,mp} = \check{G}_{l,mn} \tag{40}$$

where $p+n$ is even, $c_0=2$ and $c_n=1$ for $n>0$. Boundary conditions are treated by the tau method.

In the resulting system, $[C] \times [\bar{\Pi}] = [\check{G}]$, matrix $[C]$ consists of M band submatrices due to the decoupling of the Fourier modes. Each subsystem, $[C_m] \times [\bar{\Pi}_m] = [\check{G}_m]$, is solved using an iterative generalized Gauss–Seidel method, since elements of $[\check{G}]$ depend on elements of $[\bar{\Pi}]$ according to Eq. (38). Each complex matrix $[C_m]$ is band diagonal with order $(L+1)(N+1) \times (L+1)(N+1)$ and bandwidth $2N+3$, and is LU-decomposed once at computation start. The existence of independent subsystems favors the parallelization of the numerical solution procedure, which was realized using OpenMP directives (Hermanns, 2002). The serial version of the software requires approximately $6.5 \cdot 10^{-6}$ sec, per grid node and time-step, while the scalability factor of the parallelization is 0.75–0.85 on a 4 CPU Intel® Xeon® machine.

5. Results

5.1. Validation

The accuracy of the numerical scheme and the efficiency of the wave absorption zone were validated in Dimas and Dimakopoulos (2009) for non-breaking, cross-shore, wave propagation including comparison to corresponding results in Grilli and Horrillo (1997). The comparison is repeated here, since a direct pressure head solver of Eq. (38) was used in Dimas and Dimakopoulos (2009), while an iterative solver is used in the present application. Non-breaking waves of cross-shore propagation, period $T=5.5$, inflow wave height $H_I=0.06$ and inflow wavelength $\lambda_I=4.32$ over a constant slope beach ($\tan\beta=1/50$) are simulated. The numerical parameters are: $L_1=80$, $L_I=5$, $L_E=30$, $L_A=10$, $d_E=0.1$, $\Delta_1=0.02$, $N=32$ and $\Delta t=0.001$. The time evolution of the free-surface elevation, at four locations with corresponding water depths of $d=0.45$, $d=0.30$, $d=0.20$ and $d=0.15$, is shown in Fig. 4 and results are compared to the ones shown in Fig. 8 of Grilli and Horrillo (1997). The data in Grilli and Horrillo (1997) are presented shifted in time by an interval of 72.5 in order to compensate for the different initiation of the wave propagation and transition to the fully-developed state by the two computations. The agreement is excellent.

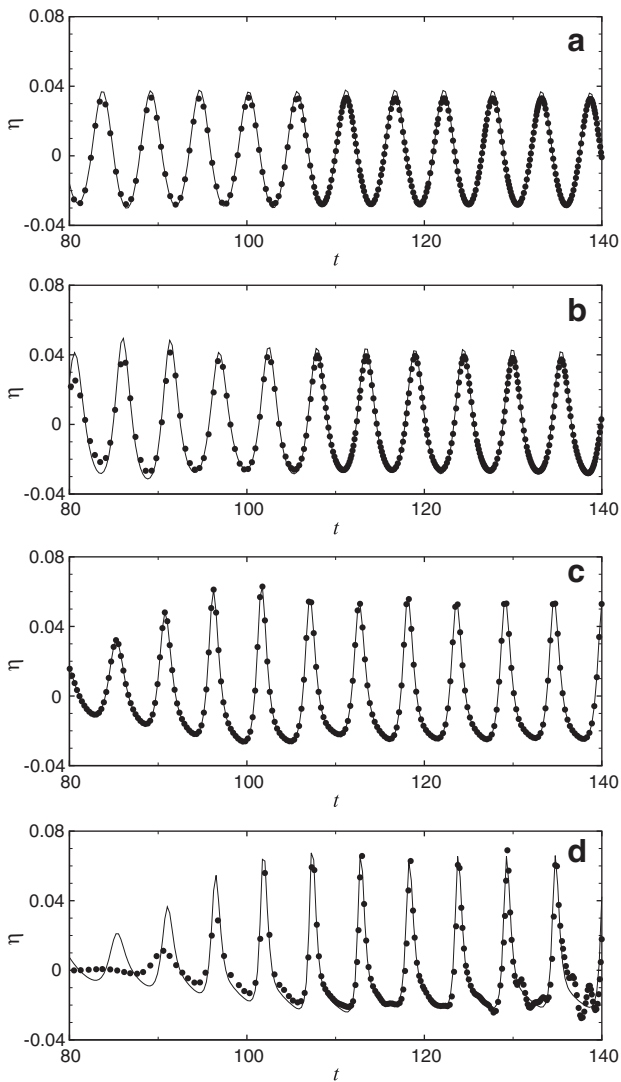


Fig. 4. Time evolution of free-surface elevation for wave propagation over beach of slope $\tan\beta=1/50$: (a) $d=0.45$, (b) $d=0.30$, (c) $d=0.20$, (d) $d=0.15$. Symbols correspond to the results in Grilli and Horrillo (1997).

Oblique wave propagation to the shore is validated by comparison to Snell's law for the refraction of linear waves. Non-breaking waves over constant slope beach ($\tan\beta=1/50$) are simulated where the dimensionless wave parameters at inflow are: $T=9.366$, $\lambda_I=8.66$, $H_I=0.001$ and angle of incidence $\varphi_I=30^\circ$. The numerical parameters are: $L_1=70$, $L_I=10$, $L_E=20$, $L_A=16$, $d_E=0.1$, $\Delta_1=0.1$, $N=32$, $M=16$, $\Delta_2=1.08$ and $\Delta t=0.01$. Refraction of wave crests is shown in Fig. 5 where the numerical prediction of the refraction angle, φ , is within $\pm 1\%$ of Snell's law.

5.2. LWS calibration

The calibration of the wave SGS model parameter, C^η , is achieved by comparison of free-surface elevation and velocity results to available experimental data (Ting and Kirby, 1994; Ting and Kirby, 1996) of cross-shore wave propagation and breaking over beach of constant slope $\tan\beta=1/35$. Three different values of the wave SGS model parameter are considered: $C^\eta=0.3$, 0.4 and 0.8 .

The dimensional flow parameters in Ting and Kirby (1994) are $d_I=0.4$ m, $T=2$ s and $H_I=0.125$ m, which correspond to wave height $H_o=0.1271$ m and wavelength $\lambda_o=6.245$ m at deep water. In our case, the same incoming wave is examined, but larger inflow depth

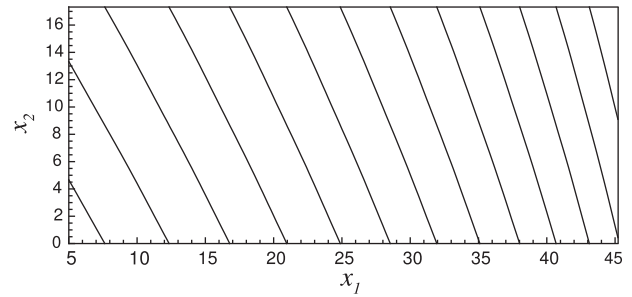


Fig. 5. Refracted crestlines of linear waves over beach of slope $1/50$, which starts at $x_1=10$, for $\varphi_I=30^\circ$.

$d_I=0.7$ m is considered, since second-order Stokes wave is imposed at inflow, and the corresponding inflow wave height is $H_I=0.1175$ m. In dimensionless form, at inflow, the wave period is $T=7.487$, which corresponds to wavelength $\lambda_I=6.605$, and the wave height is $H_I=0.168$. The Iribaren number, $\xi_o = \tan\beta\sqrt{\lambda_o}/H_o = 0.2$, corresponds to medium strength spilling breaker. The computational domain overall length is $L_1=72$, the inflow length is $L_I=15$, the outflow length and depth are $L_E=23.05$ and $d_E=0.03$, respectively, and the absorption zone length is $L_A=15$. The numerical parameters are: $\Delta_1=0.04$, $N=64$, $M=32$, $\Delta_2=0.02$ and $\Delta t=0.0001$. The smallest resolved scale is set by $\Delta = (\Delta_1\Delta_2\Delta_3)^{1/3}$ where $\Delta_3=2/N$ is the average spacing of the Chebyshev collocation points.

In Fig. 6, snapshots of the resolved free-surface elevation, at several time instants after 20 wave periods, are presented for $C^\eta=0.4$, and compared to experimental data of maximum (crest) and minimum (trough) values of free-surface elevation (Ting and Kirby, 1994). The comparison shows that the LWS predicts accurately the incipient breaking parameters (wave height and depth) and the wave dissipation rate in the outer surf zone, while it overestimates the wave dissipation rate in the inner surf zone. In Fig. 7, the distribution of wave height is

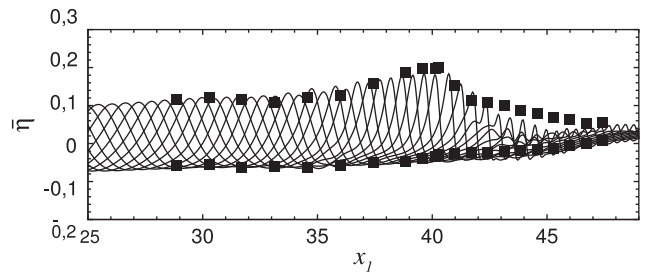


Fig. 6. Free-surface elevation at several time instants, during shoaling and in the surf zone, over beach of slope $1/35$, which starts at $x_1=15$, for $C^\eta=0.4$. Symbols correspond to experimental data of the free-surface elevation envelope (Ting and Kirby, 1994).

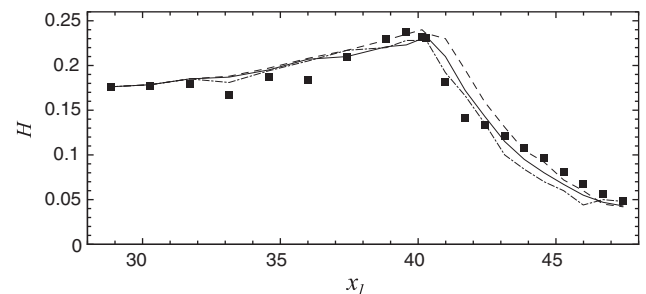


Fig. 7. Wave height distribution, during shoaling and in the surf zone, over beach of slope $1/35$, for $C^\eta=0.3$ (dashed line), $C^\eta=0.4$ (solid line) and $C^\eta=0.8$ (dash-dot line). Symbols correspond to experimental data (Ting and Kirby, 1994).

presented, during shoaling and in the surf zone, for the three different values of the wave SGS model parameter, $C^\eta = 0.3, 0.4$ and 0.8 , and compared to corresponding experimental data (Ting and Kirby, 1994). During shoaling, the LWS prediction of monotonic wave height increase is typical of other numerical studies (Christensen, 2006; Hieu et al., 2004; Zhao et al., 2004), as well. For SGS parameter $C^\eta = 0.4$, the predicted breaking wave height ($H_b = 0.233$) and depth ($d_b = 0.28$) are in excellent agreement with the experimental data. For $C^\eta = 0.3$ and $C^\eta = 0.8$, LWS results of breaking wave height deviate from experimental data by +3% ($H_b = 0.240$) and -2% ($H_b = 0.229$), respectively, while breaking depth is underpredicted by 7.7% ($d_b = 0.26$) for $C^\eta = 0.3$. In the outer surf zone ($d/d_b > 0.75$), wave dissipation is better captured for $C^\eta = 0.8$, while in the inner surf zone, wave dissipation is better predicted for $C^\eta = 0.3$. The best balanced behavior is achieved for $C^\eta = 0.4$.

The normalized, zero-mean, phase-averaged flow velocity components, defined as $U'_i = (U_i - U_{im}) / \sqrt{gd_b}$ where U_i is the phase-averaged velocity and U_{im} is the mean velocity, are shown in Fig. 8 at $d/d_b = 0.775$ ($x_1 = 42.67$), which corresponds to the second measurement location of Ting and Kirby (1996) in the surf zone. In our computations, averaging starts 10 wave periods after the first breaking wave and lasts for 4 periods. The LWS results agree very well with the experimental data.

In LWS, wave breaking and dissipation in the surf zone are anticipated to be generated by the combined action of wave and eddy SGS stresses. In Fig. 9, the envelope of the SGS stress components in x_1 and x_3 , during shoaling and in the surf zone, is shown; the SGS stress components in x_2 are not shown since they are much weaker. In LWS, the growth and action of the SGS stresses depend physically on the flow state and are accomplished automatically without empirical criteria or additional parameters. It is observed that the most active, at inducing wave breaking and causing wave dissipation in the surf zone, are the wave SGS stresses and, especially, the τ_{13}^{η} component. The wave SGS stresses become substantial during shoaling at $d/d_b \approx 1.2$, reach their maximum strength in the surf zone at $d/d_b \approx 0.8$ (about

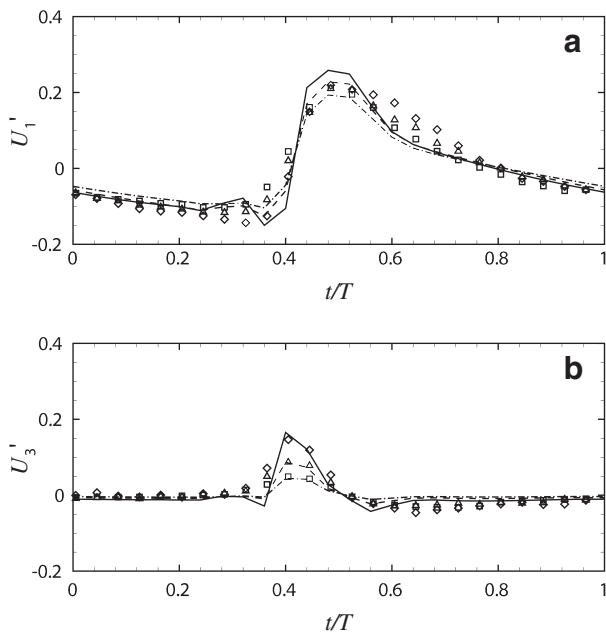


Fig. 8. Normalized, zero-mean, phase-averaged velocity, $U'_i = (U_i - U_{im}) / \sqrt{gd_b}$, over beach of slope 1/35, at $d/d_b = 0.775$, for $C^\eta = 0.4$: (a) horizontal and (b) vertical component. Lines correspond to LWS results and symbols to experimental data (Ting and Kirby, 1994) at three different depths along x_3 : (i) $x_3/d = 0.26$ (solid line and diamonds), (ii) $x_3/d = 0.53$ (dashed line and triangles) and (iii) $x_3/d = 0.72$ (dot-dash line and squares).

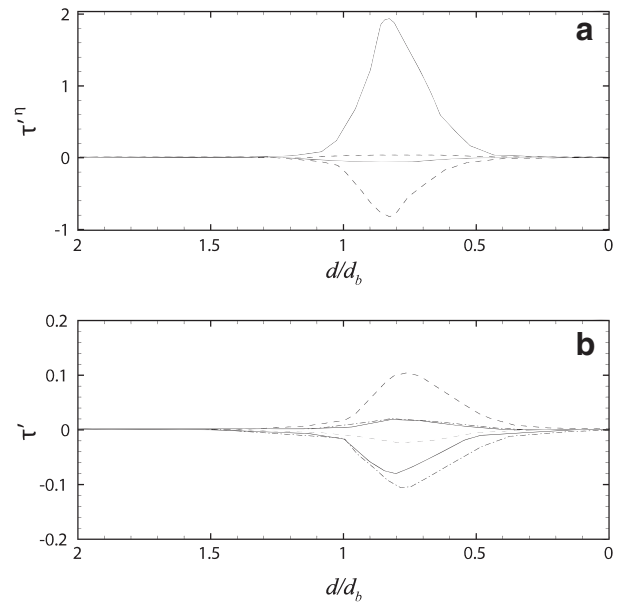


Fig. 9. Envelope of normalized SGS stresses, $[\tau', \tau''^\eta] = [\tau, \tau''] / (\rho g d_b \tan \beta)$, during shoaling and in the surf zone, over beach of slope 1/35, for $\varphi_1 = 0^\circ$: (a) wave SGS stresses τ_{13}^η (solid lines) and τ_{33}^η (dashed lines), and (b) eddy SGS stresses τ_{13} (solid Fig. lines), τ_{11} (dashed lines) and τ_{33} (dash-dot lines).

0.3T after breaking) and become small again for $d/d_b \leq 0.4$. Typical instantaneous contours of the dominant wave SGS stress, τ_{13}^η , at a cross-section ($x_2 = 0.32$) in the surf zone, are shown in Fig. 10. The three snapshots correspond to incipient breaking, and 0.3T and T after breaking. The particular SGS stress component develops in the vicinity of the breaking wavefront and its distribution along x_3 exhibits a maximum at the free surface where the effect of SGS free-surface undulations is strongest.

Typical snapshots of the spanwise vorticity component, ω_2 , at a cross-section ($x_2 = 0.32$) in the surf zone, are shown in Fig. 11. Vorticity production emanates at the breaking wavefront (crest at $x_1 = 40.2$ in Fig. 11a). At time 0.3T after breaking, the vorticity distribution in Fig. 11c indicates the full development of the surface roller underneath the breaking wavefront where $d/d_b = 0.8$ (crest at $x_1 = 42.2$). This transition time, from incipient breaking to a fully-developed surface roller, is in agreement to the corresponding time, from incipient breaking to a fully-turbulent wave crest, according to Duncan et al. (1999). The same value (0.3T) is also used, as a roller growth time parameter, in Dimas and Dimakopoulos (2009) with successful results. It is also apparent that the roller formation is directly related to the growth of the wave SGS stresses in the interval $1 \geq d/d_b \geq 0.8$. Downstream of the fully-developed roller, there is a

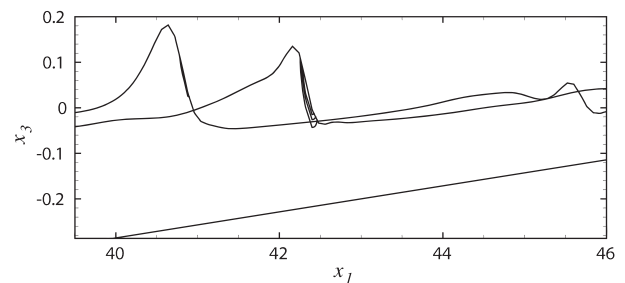


Fig. 10. Wave SGS stress τ_{13}^η , at a cross-section ($x_2 = 0.32$) in the surf zone, over beach of slope 1/35, for $\varphi_1 = 0^\circ$. Wave crests correspond to incipient breaking, and 0.3T and T after breaking. Contours are at equal intervals of 0.004 from 0 to 0.012.

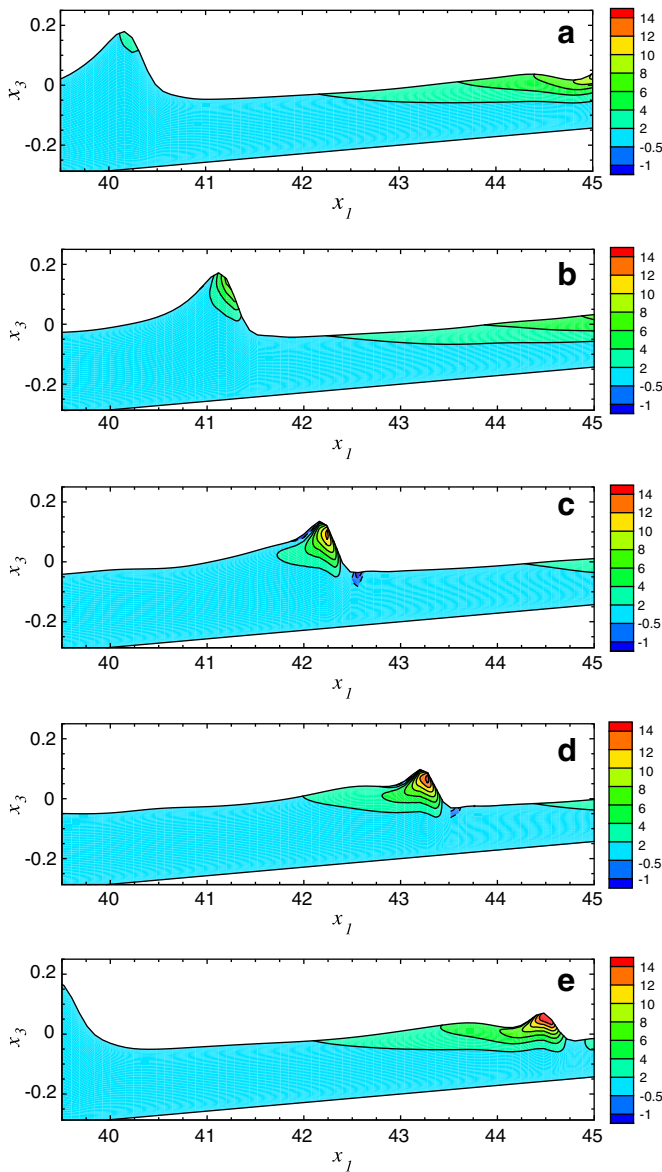


Fig. 11. Spanwise vorticity, at a cross-section ($x_2 = 0.32$) in the surf zone, over beach of slope 1/35, for $\varphi_i = 0^\circ$. Snapshot (a) corresponds to incipient breaking and (c) to time $0.3T$ after breaking.

negative secondary vortex, which was also observed in [Dabiri and Gharib \(1997\)](#), and the ratio of peak vorticity magnitude in the roller to the one in the secondary vortex is about equal to 14.

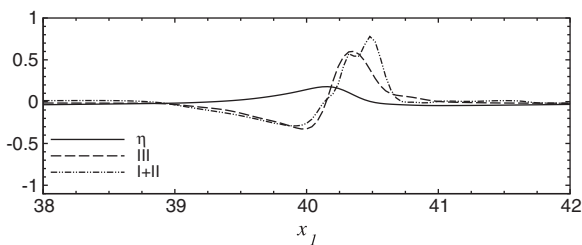


Fig. 12. Contribution to vorticity flux, at a cross-section ($x_2 = 0.32$) in the surf zone, over beach of slope 1/35, for $\varphi_i = 0^\circ$, by the advection (I+II) and gravity (III) terms of Eq. (41) at incipient breaking (same as in Fig. 11a).

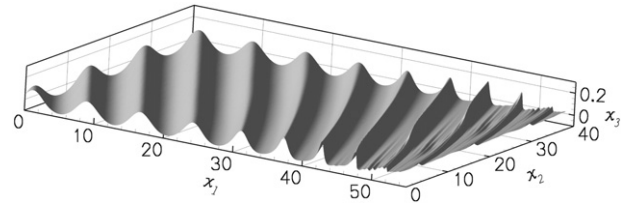


Fig. 13. Snapshot of free-surface elevation in the surf zone over beach of slope 1/35, which starts at $x_1 = 20$, for $\varphi_i = 30^\circ$.

According to [Rood \(1994\)](#), the flux of vorticity ω_2 (in our notation), at the free surface, is

$$\frac{1}{R} \left(\frac{\partial \omega_2}{\partial r} \right)_{r=0} = \underbrace{\frac{\partial u_s}{\partial t}}_I + \underbrace{u_s \frac{\partial u_s}{\partial s}}_{II} + \underbrace{\frac{\cos \theta}{F^2}}_{III} \quad (41)$$

where R is the Reynolds number, r and s are the curvilinear coordinates perpendicular (outwards) and tangent (in the wave propagation direction) to the free surface, respectively, u_s is the velocity component along s , and θ is the angle between the free surface and the gravity direction. According to Eq. (41), the flux of vorticity is due to the sum of the advection (I+II) and the gravity (III) terms. For steady spilling breakers and weak hydraulic jumps, where $\partial u_s / \partial t \approx 0$, the experimental results in [Dabiri and Gharib \(1997\)](#) and [Misra et al. \(2008\)](#) indicate that the dominant mechanism for vorticity flux at the free surface is the convective term II (flow deceleration) of Eq. (41). In our unsteady breakers, though, term I is nonzero. A typical snapshot of the distribution, in the surf zone, of the advection (I+II) and the gravity (III) terms of Eq. (41), at incipient breaking, is shown in Fig. 12. Apparently, at incipient breaking, advection and gravity contribute equally to the vorticity flux, and only later, after the roller has been fully-developed, the contribution by the advection term becomes stronger. Therefore, steady spilling breakers and weak hydraulic jumps do not present a good description of unsteady breaking early in the process but only after the surface roller has been fully developed in the inner surf zone.

After the development of the roller, its peak vorticity magnitude remains more or less constant and the breaker moves like a bore (Fig. 11d–e) till it reaches a depth of $d/d_b \approx 0.5$. This behavior was also reported in [Watanabe and Mori \(2008\)](#). During that phase, vorticity is advected in the wake of the surface roller and diffused, by turbulence, towards the bed. The weaker vorticity in the wake of past surface rollers remains for more than a wave period in the surf zone, thus interacting with subsequent breaking waves. Close to the bed, our model predicts a weak vorticity presence, due to the absence of no-slip condition, while in other studies ([Briganti et al., 2004](#)) the vorticity there is negligible.

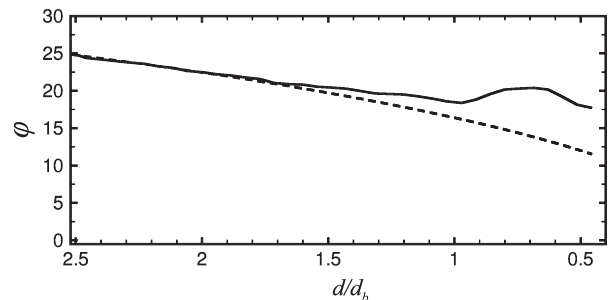


Fig. 14. Propagation angle variation, during shoaling and in the surf zone, over beach of slope 1/35, for $\varphi_i = 30^\circ$, by LWS (solid line) and Snell's law (dashed line).

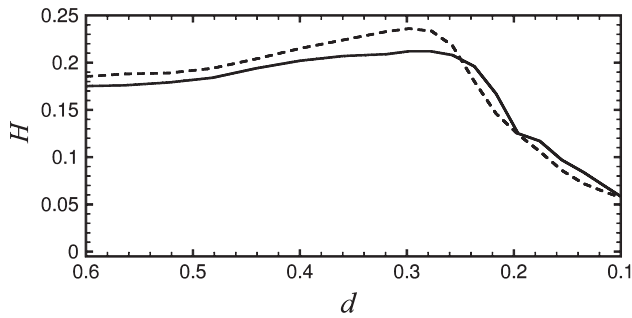


Fig. 15. Wave height distribution, during shoaling and in the surf zone, over beach of slope 1/35, for $\varphi_l=0^\circ$ (dashed line) and $\varphi_l=30^\circ$ (solid line). Incoming waves have identical height and period.

5.3. Oblique breaking waves

Three-dimensional simulation of spilling breaking over constant slope beach ($\tan\beta=1/35$) is also performed for oblique wave propagation to the shoreline. Inflow incidence angle is $\varphi_l=30^\circ$, which corresponds to $\varphi_o=42.4^\circ$ in deep water. All other inflow wave and numerical parameters, including the model parameters $C=0.1$ and $C^\eta=0.4$, are as in the calibration case for $\varphi_l=0^\circ$, with the exceptions of $M=64$ and $\Delta_2=0.206$ in the spanwise direction, and inflow length, $L_l=20$.

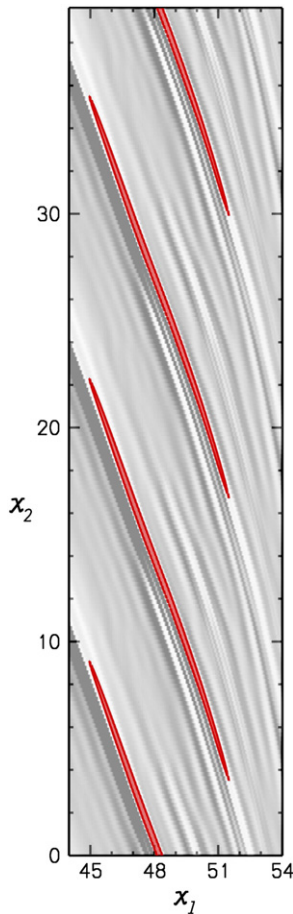


Fig. 16. Plan view of free-surface elevation (grayscale) and isosurface (red) of the magnitude of the wave SGS stresses, $((\tau_{13}^i)^2 + (\tau_{23}^i)^2 + (\tau_{33}^i)^2)^{1/2} = 0.0005$, in the surf zone over beach of slope 1/35, for $\varphi_l=30^\circ$. Breaking point is at $x_1=46.25$.

The spanwise width of the computational domain is equal to one spanwise wavelength to facilitate the use of periodic boundary conditions in x_2 .

Typical instantaneous free-surface elevation is shown in Fig. 13 where the spanwise width of the snapshot includes three wavelengths, by exploiting the periodicity in x_2 , for clarity of the exposition. The simultaneous nonlinear refraction and shoaling of waves is observed, as well as the gradual breaking of wave crestlines when they reach breaking depth. The variation of the propagation angle, due to refraction and breaking, is shown in Fig. 14. The spanwise-averaged angle is computed at the zeroing of the free-surface elevation upstream of the wave crest, and compared to Snell's law. During shoaling, the angle predicted by the nonlinear simulation is larger than the one of linear theory, while in the surf zone, the angle does not decrease beyond its value at breaking. The distribution of spanwise-averaged wave height, due to refraction and shoaling in the outer zone and dissipation in the surf zone, is shown in Fig. 15. As expected, the breaking wave height, $H_b=0.21$, and the breaking depth, $d_b=0.25$, for $\varphi_l=30^\circ$ are smaller compared to the ones for $\varphi_l=0^\circ$.

A plan-view of the instantaneous free-surface elevation and an isosurface of the magnitude of the wave SGS stresses is shown in Fig. 16. Three spanwise wavelengths are shown for clarity. The development of the wave SGS stresses at the breaking wavefront is related to the production of vorticity and the creation of the surface roller, and this procedure starts and evolves automatically without empirical criteria or additional parameters. As in the cross-shore case, the growth of the wave SGS stresses emanates just before the breaking depth. Typical contours of the dominant wave SGS stresses,

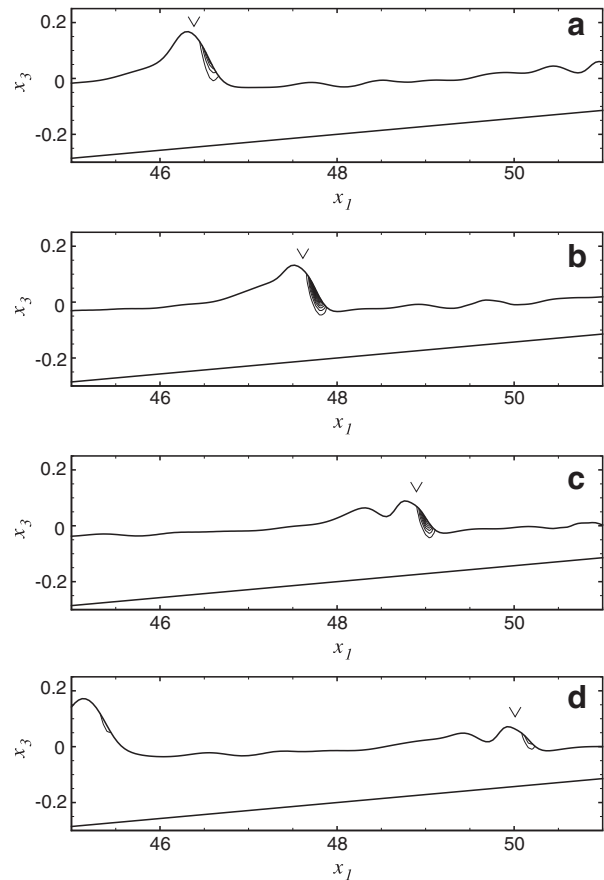


Fig. 17. Wave SGS stress τ_{13}^i , at four cross-sections in the surf zone, over beach of slope 1/35, for $\varphi_l=30^\circ$: (a) $x_2=9.909$, (b) $x_2=6.606$, (c) $x_2=3.303$, (d) $x_2=0$. Contours are at equal intervals of 0.0005 from 0 to 0.007.

τ_{13}^j and τ_{23}^j , at four cross-sections along x_2 in the surf zone, are shown in Figs. 17 and 18. The particular SGS stress components develop in the vicinity of the breaking wavefront and their distribution along x_3 exhibit a maximum at the free surface where the effect of SGS free-surface undulations is strongest.

A plan-view of the instantaneous free-surface elevation and two isosurfaces of the vorticity magnitude is shown in Fig. 19. Three spanwise wavelengths are shown for clarity. The surface roller, identified by the isosurface of value 10 in Fig. 19, extends for about three spanwise wavelengths, and follows the orientation of the breaking wave crests. Vorticity generation emanates at breaking and is advected in the breaker wake mainly along the spanwise direction as shown by the isosurface of value 6 in Fig. 19. The advected vorticity is not dissipated during a wave period, and, therefore, interacts with the next oncoming spilling breaker. Typical contours of spanwise and streamwise vorticity, ω_2 and ω_1 , respectively, at four cross-sections along x_2 in the surf zone, are shown in Figs. 20 and 21. Spanwise vorticity is mainly clockwise, while streamwise is counter-clockwise. It is observed that spanwise and streamwise vorticity exhibit a similar distribution underneath the breaking wavefront. At $d/d_b = 0.8$, maximum values for ω_2 and ω_1 are 10.6 and -3.9 , respectively. The existence of two significant components of vorticity is another indication that the surface roller is an oblique to the shoreline structure. By considering the average ratio of these components in the roller area, for $d/d_b = 0.8$, the surface roller is obliquely orientated to the shoreline at angle 20° , which is about equal to the propagation angle in the surf zone. Vertical vorticity, ω_3 , is insignificant compared to the other two components, and its magnitude does not exceed the value of 0.5.

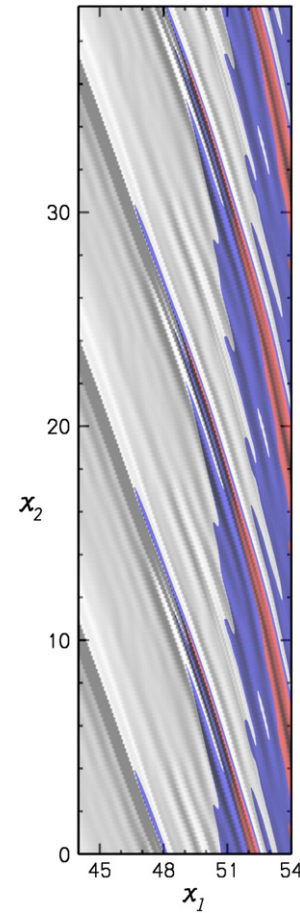


Fig. 19. Plan view of free-surface elevation (grayscale) and isosurfaces of the vorticity magnitude of values 6 (blue) and 10 (red) in the surf zone over beach of slope 1/35, for $\varphi_l = 30^\circ$. Breaking point is at $x_1 = 46.25$.

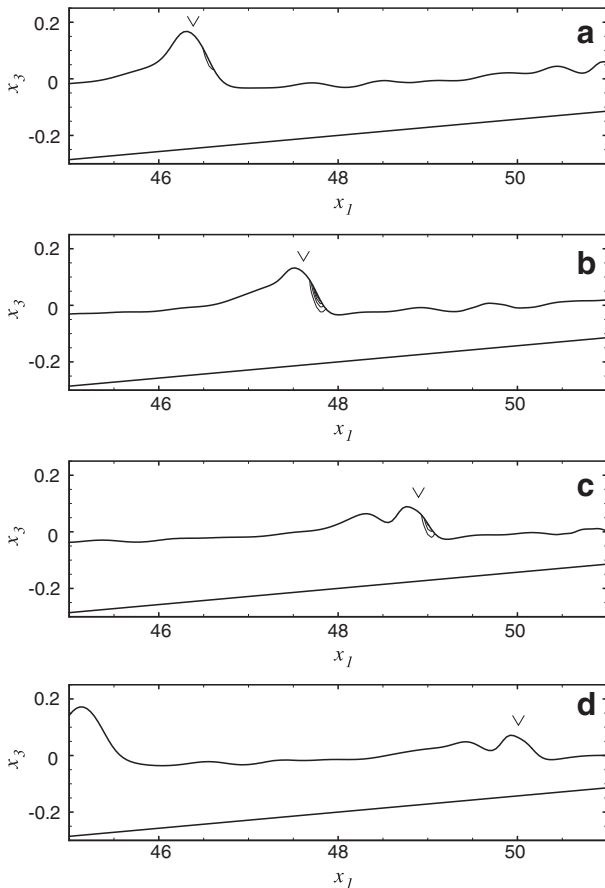


Fig. 18. Wave SGS stress τ_{23}^j , at four cross-sections in the surf zone, over beach of slope 1/35, for $\varphi_l = 30^\circ$: (a) $x_2 = 9.909$, (b) $x_2 = 6.606$, (c) $x_2 = 3.303$, (d) $x_2 = 0$. Contours are at equal intervals of 0.0005 from 0 to 0.0025.

6. Conclusions

A numerical model for cross-shore and oblique wave propagation and breaking in the coastal zone was presented based on the concept of LWS, and applied for a beach of constant slope ($\tan\beta = 1/35$). According to the method, the large scales of velocity, pressure and free-surface elevation are resolved, while the effect of the corresponding small scales is accounted for by eddy and wave SGS stress model; herein a Smagorinsky-type eddy viscosity model. The model may be not fully applicable in very shallow water, where the turbulent free-surface oscillation is of the same order with the water depth, thus limiting its performance close to the shoreline. The model calibration was achieved by comparison to available experimental data (Ting and Kirby, 1994, 1996) for cross-shore spilling breaking, and the values of the model parameters were used for oblique breaking as well. This model is suited to spilling breakers, but a more advanced, probably dynamic, SGS stress model will be required for plunging breakers.

For both cross-shore and oblique wave propagation in the outer zone, breaking and dissipation in the surf zone, it was found that the wave SGS stresses are at least one order of magnitude larger than the eddy ones, while their development requires no empirical criteria or additional parameters. Their action is stronger in the area under the breaking wavefront, in accordance to the effect of SGS free-surface undulations, and generates appropriate vorticity, which evolves into the formation of the surface roller. At incipient breaking, both advection and gravity contribute to the vorticity flux at the free surface, while only after the full development of the surface roller, the

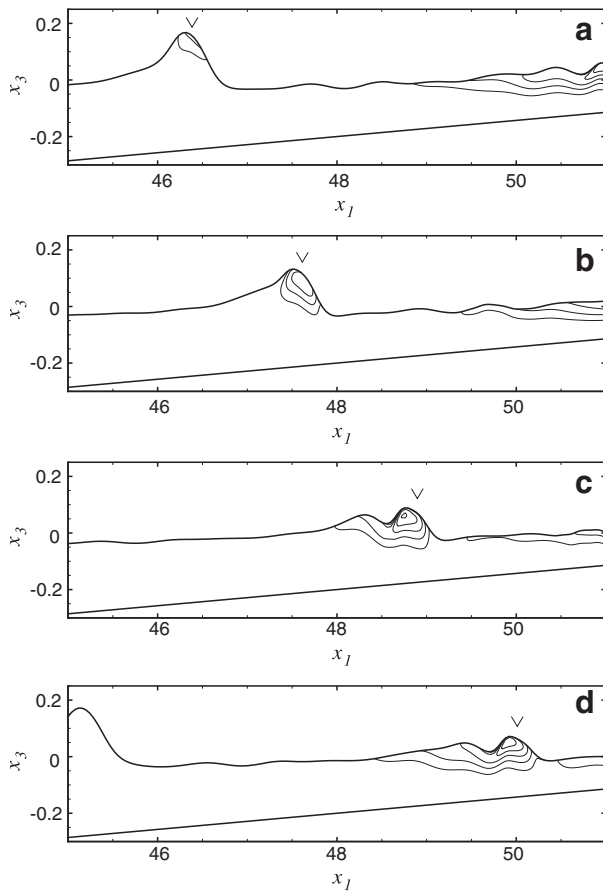


Fig. 20. Spanwise vorticity, ω_2 , at four cross-sections in the surf zone, over beach of slope 1/35, for $\varphi_1 = 30^\circ$: (a) $x_2 = 9.909$, (b) $x_2 = 6.606$, (c) $x_2 = 3.303$, (d) $x_2 = 0$. Contours are at equal intervals of 2 from 0 to 10.

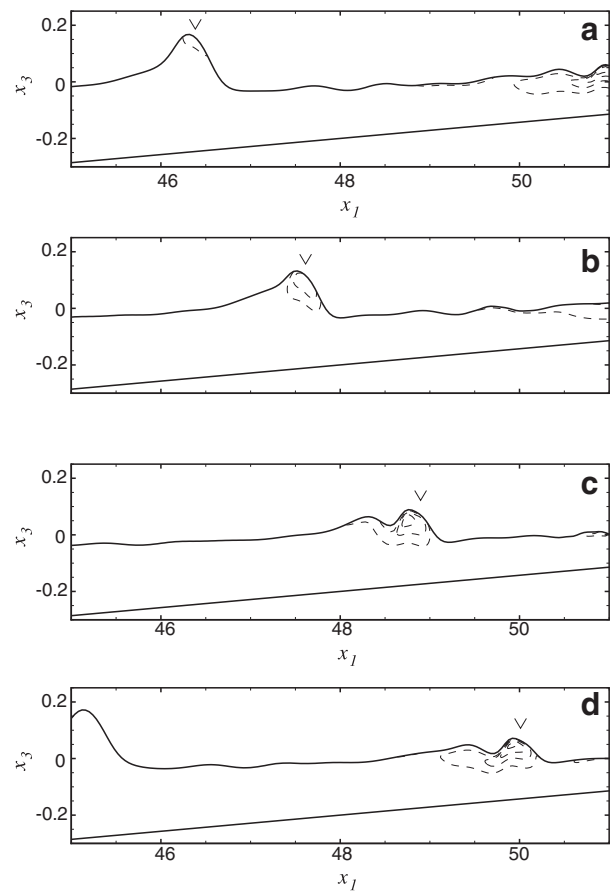


Fig. 21. Streamwise vorticity, ω_1 , at four cross-sections in the surf zone, over beach of slope 1/35, for $\varphi_1 = 30^\circ$: (a) $x_2 = 9.909$, (b) $x_2 = 6.606$, (c) $x_2 = 3.303$, (d) $x_2 = 0$. Contours are at equal intervals of 1 from -4 to 0.

effect of advection becomes stronger. For oblique waves, the model captures the gradual breaking and dissipation of the wave crestlines in the surf zone, while the advection of vorticity in the breaker wake is mainly in the spanwise direction.

Acknowledgments

This paper is part of the 03ED617 research project, implemented within the framework of the “Reinforcement Programme of Human Research Manpower” (PENED) and co-financed by National and Community Funds (10% from the Patras Port Authority, 18% from the Greek Ministry of Development-General Secretariat of Research and Technology and 72% from the E.U.-European Social Fund). We also thank Mr. Gerasimos Kolokithas, PhD candidate at our Hydraulic Engineering Laboratory, for his helpful contribution on the simulation software development.

References

- Battjes, J.A., 1988. Surf-zone dynamics. *Annu. Rev. Fluid Mech.* 20, 257–291.
- Bradford, S.F., 2000. Numerical simulation of surf zone dynamics. *J. Waterway, Port, Coastal Ocean Eng.* 126 (1), 1–13.
- Briganti, R., Musumeci, R.E., Bellotti, G., Brocchini, M., Foti, E., 2004. Boussinesq modeling of breaking waves: description of turbulence. *J. Geophys. Res.* 109, C07015.
- Brocchini, M., Peregrine, D.H., 2001a. The dynamics of strong turbulence at free surfaces. Part 1. Description. *J. Fluid Mech.* 449, 225–254.
- Brocchini, M., Peregrine, D.H., 2001b. The dynamics of strong turbulence at free surfaces. Part 2. Free-surface boundary conditions. *J. Fluid Mech.* 449, 255–290.
- Choi, J., Yoon, S.B., 2009. Numerical simulations using momentum source wave-maker applied to RANS equation model. *Coast. Eng.* 56 (10), 1043–1060.
- Christensen, E.D., 2006. Large eddy simulation of spilling and plunging breakers. *Coast. Eng.* 53 (5–6), 463–485.

- Christensen, E.D., Deigaard, R., 2001. Large eddy simulation of breaking waves. *Coast. Eng.* 42 (1), 53–86.
- Cointe, R., Tulin, M.P., 1994. Theory of steady breakers. *J. Fluid Mech.* 276, 1–20.
- Dabiri, D., Gharib, M., 1997. Experimental investigation of the vorticity generation within a spilling water wave. *J. Fluid Mech.* 330, 113–139.
- de Serio, F., Mossa, M., 2006. Experimental study on the hydrodynamics of regular breaking waves. *Coast. Eng.* 53 (1), 99–113.
- Dimakopoulos, A., 2009. Numerical simulation of the three-dimensional turbulent flow induced by breaking waves in the coastal surf zone (in greek). Ph.D. thesis, University of Patras, Patras, Greece.
- Dimas, A.A., Dimakopoulos, A.S., 2009. A surface roller model for the numerical simulation of spilling wave breaking constant slope beach. *J. Waterway, Port, Coastal Ocean Eng.* 135 (5), 235–244.
- Dimas, A.A., Fialkowski, L.T., 2000. Large-wave simulation (LWS) of free-surface flows developing weak spilling breaking waves. *J. Comput. Phys.* 159 (2), 172–196.
- Duncan, J.H., 1983. The breaking and non-breaking resistance of two-dimensional hydrofoil. *J. Fluid Mech.* 126, 507–520.
- Duncan, J.H., Qiao, H., Philomin, V., Wenz, A., 1999. Gentle spilling breakers: crest profile evolution. *J. Fluid Mech.* 379, 191–222.
- Godlieb, D., Orszag, S.A., 1977. Numerical Analysis of Spectral Methods. SIAM, Philadelphia.
- Grilli, S.T., Horrillo, J., 1997. Numerical generation and absorption of fully nonlinear periodic waves. *J. Eng. Mech.* 123 (10), 1060–1069.
- Harlow, F.H., Welch, J.E., 1965. Numerical calculation of time-dependent viscous incompressible flow of fluid with free surface. *Phys. Fluids* 8, 2182–2189.
- Hermanns, M., 2002. Parallel Programming in Fortran 95 Using OpenMP. www.openmp.org/presentations/miguel/F95_OpenMPv1_v2.pdf.
- Hieu, P.D., Tanimoto, K., Ca, V.T., 2004. Numerical simulation of breaking waves using a two-phase flow model. *Appl. Math. Modelling* 28 (11), 983–1005.
- Hirt, C.W., Nichols, B.D., 1981. Volume of fluid (VOF) method for the dynamics of free boundaries. *J. Comput. Phys.* 39 (1), 201–225.
- Huang, Z.-C., Hsiao, S.-C., Hwung, H.-H., Chang, K.-A., 2009. Turbulence and energy dissipations of surf-zone spilling breakers. *Coast. Eng.* 56 (7), 733–746.
- Karambas, T.V., Koutitas, C., 1992. A breaking wave propagation model based on the Boussinesq equations. *Coast. Eng.* 18 (1–2), 1–19.
- Kennedy, A.B., Chen, Q., Kirby, J.T., Dalrymple, R.A., 2000. Boussinesq modelling of wave transformation, breaking and runup. I: 1D. *J. Waterway, Port, Coastal Ocean Eng.* 126 (1), 39–47.

- Lin, P., Liu, P.L.-F., 1998. A numerical study of breaking waves in the surf zone. *J. Fluid Mech.* 359, 239–264.
- Lin, P., Liu, P.L.-F., 1999. Internal wave-maker for Navier–Stokes equations models. *J. Waterway, Port, Coastal Ocean Eng.* 125 (4), 207–215.
- Longo, S., 2009. Vorticity and intermittency within the pre-breaking region of spilling breakers. *Coast. Eng.* 56 (3), 285–296.
- Madsen, P.A., Sorensen, O.R., Schäffer, H.A., 1997. Surf zone dynamics simulated by a Boussinesq type model. Part I. Model description and cross-shore motion of regular waves. *Coast. Eng.* 32 (4), 255–287.
- Misra, S.K., Kirby, J.T., Brocchini, M., Veron, F., Thomas, M., Kambhamettu, C., 2008. The mean and turbulent flow structure of a weak hydraulic jump. *Phys. Fluids* 20 (035106), 1–21.
- Musumeci, R.E., Svendsen, I.A., Veeramony, J., 2005. The flow in the surf zone: a fully nonlinear Boussinesq-type of approach. *Coast. Eng.* 52 (7), 565–598.
- Okamoto, T., Basco, D.R., 2006. The Relative Trough Froude Number for initiation of wave breaking: theory, experiments and numerical model confirmation. *Coast. Eng.* 53 (8), 675–690.
- Peregrine, D.H., 1983. Breaking waves on beaches. *Annu. Rev. Fluid Mech.* 15, 149–178.
- Press, W.H., Teukolsky, S.A., Vetterling, W.T., Flannery, B.P., 1992. *Numerical Recipes in Fortran. The Art of Scientific Computing*, 2nd Edition. Cambridge University Press, Cambridge.
- Rogallo, R.S., Moin, P., 1984. Numerical simulation of turbulent flows. *Annu. Rev. Fluid Mech.* 16, 99–137.
- Rood, E.P., 1994. Interpreting vortex interactions with a free surface. *J. Fluids Eng.* 116, 91–94.
- Schäffer, H.A., Madsen, P.A., Deigaard, R., 1993. A Boussinesq model for waves breaking in shallow water. *Coast. Eng.* 20 (3–4), 185–202.
- Ting, F.C.K., Kirby, J.T., 1994. Observation of undertow and turbulence in a laboratory surf zone. *Coast. Eng.* 24 (1–2), 51–80.
- Ting, F.C.K., Kirby, J.T., 1996. Dynamics of surf-zone turbulence in a spilling breaker. *Coast. Eng.* 27 (3–4), 131–160.
- Torres-Freyermuth, A., Losada, I.J., Lara, J.L., 2007. Modeling of surf zone processes on a natural beach using Reynolds-Averaged Navier–Stokes equations. *J. Geophys. Res.* 112, C09014.
- Veeramony, J., Svendsen, I.A., 2000. The flow in surf-zone waves. *Coast. Eng.* 39 (1–2), 93–122.
- Watanabe, Y., Mori, N., 2008. Infrared measurements of surface renewal and subsurface vortices in nearshore breaking waves. *J. Geophys. Res.* 113, C07015.
- Watanabe, Y., Saeki, H., Hosking, R.J., 2005. Three-dimensional vortex structures under breaking waves. *J. Fluid Mech.* 545, 291–328.
- Zhao, Q., Armfield, S., Tanimoto, K., 2004. Numerical simulation of breaking waves by a multi-scale turbulence model. *Coast. Eng.* 51 (1), 53–80.